Cell, Vol. 119, 393–405, October 29, 2004, Copyright ©2004 by Cell Press

Structural Analysis of Autoinhibition in the Ras Activator Son of Sevenless

Holger Sondermann,[1,2,5] Stephen M. Soisson,[3,5,6] Sean Boykevisch,[4] Shao-Song Yang,[4] Dafna Bar-Sagi,[4] and John Kuriyan[1,2,*]

[1]Howard Hughes Medical Institute
Department of Molecular and Cell Biology and
Department of Chemistry
University of California, Berkeley and
[2]Physical Biosciences Division
Lawrence Berkeley National Laboratory
Berkeley, California 94720
[3]Laboratories of Molecular Biophysics
The Rockefeller University
1230 York Avenue
New York, New York 10021
[4]Department of Molecular Genetics
and Microbiology
The State University of New York at Stony Brook
Stony Brook, New York 11794

Summary

The classical model for the activation of the nucleotide exchange factor Son of sevenless (SOS) involves its recruitment to the membrane, where it engages Ras. The recent discovery that Ras•GTP is an allosteric activator of SOS indicated that the regulation of SOS is more complex than originally envisaged. We now present crystallographic and biochemical analyses of a construct of SOS that contains the Dbl homology-pleckstrin homology (DH-PH) and catalytic domains and show that the DH-PH unit blocks the allosteric binding site for Ras and suppresses the activity of SOS. SOS is dependent on Ras binding to the allosteric site for both a lower level of activity, which is a result of Ras•GDP binding, and maximal activity, which requires Ras•GTP. The action of the DH-PH unit gates a reciprocal interaction between Ras and SOS, in which Ras converts SOS from low to high activity forms as Ras•GDP is converted to Ras•GTP by SOS.

Introduction

The signaling protein Ras is a molecular switch that cycles between inactive GDP bound and active GTP bound states (Vetter and Wittinghofer, 2001). Receptors that signal through tyrosine kinases activate Ras by recruiting the Ras-specific nucleotide exchange factor Son of sevenless (SOS) to the plasma membrane, where SOS and Ras form a complex that results in the expulsion of otherwise tightly bound nucleotides from Ras (Yarden and Sliwkowski, 2001; Nimnual and Bar-Sagi, 2002; Boriack-Sjodin et al., 1998). Ras is kept under strict control in the cell, and the unregulated activation of Ras is a consistent hallmark of many cancers (Coleman et al., 2004).

SOS is a complex multidomain protein of about 1330 residues (Figure 1A). The N-terminal domain (~200 residues) contains two tandem histone folds of unknown function (Sondermann et al., 2003) and is followed by a Dbl homology (DH) domain (~200 residues) and a pleckstrin homology (PH) domain (~150 residues) that together are implicated in the activation of the small GTPase Rac1 (Nimnual et al., 1998; Soisson et al., 1998). The next two domains are both required for the Ras-specific nucleotide exchange activity of SOS and are always found together in other Ras-specific nucleotide exchange factors. The first of these is the Ras exchanger motif (Rem) domain (~200 residues), which is followed by the Cdc25 domain (~300 residues; named for homology to Cdc25, the Ras activator protein in yeast) (Boriack-Sjodin et al., 1998). We refer to these two domains together as SOS^{cat}. Finally, the ~250 residues in the C-terminal region provide docking sites for adaptor proteins such as Grb2 (Buday and Downward, 1993; Egan et al., 1993; Gale et al., 1993; Li et al., 1993).

The structure of nucleotide-free Ras in complex with SOS^{cat} showed that Ras is bound in such a way that its nucleotide binding site is almost completely disrupted (Boriack-Sjodin et al., 1998). The interaction between Ras and SOS is localized entirely to the Cdc25 domain, and the position and function of the Rem domain, which interacts with a surface of the Cdc25 domain that is distal to the active site, was puzzling at first. A recent crystallographic study uncovered a role for the Rem domain in a previously unsuspected allosteric mechanism in SOS (Margarit et al., 2003). Ras•GTP, the product of the exchange reaction, interacts with a distal binding site on SOS^{cat} that is between the Rem and Cdc25 domains, thereby forming a bridge between these two domains (Figure 1A). Binding of Ras•GTP to this distal allosteric site results in increased Ras exchange activity, indicating the presence of a positive feedback loop in the activation of Ras by SOS.

Initial models for the regulation of SOS emphasized its recruitment to the membrane as the key step of activation, since Ras is membrane bound. The regulation of SOS is likely to be more complex than simple membrane recruitment. In addition to the Grb2-mediated recruitment of SOS to the plasma membrane, early experiments suggested a role for the N-terminal segment of SOS in its activation (Byrne et al., 1996). Deletion of the C-terminal docking segment or the N-terminal 550 amino acids (including the histone domain and the DH-PH unit) increases SOS activity in cellular assays (Corbalan-Garcia et al., 1998; Kim et al., 1998; Qian et al., 1998). These results, as well as a recent genetic study of *Drosophila* SOS (Silver et al., 2004), suggest that there is a complex but poorly characterized interplay between the domains of SOS that results in modulation of the ability of SOS to activate Ras (Hall et al., 2002).

In the present study, we investigate a construct of SOS ($SOS^{DH\text{-}PH\text{-}cat}$) that contains the DH-PH unit in addition to the catalytic unit (SOS^{cat}). By determining the structure

*Correspondence: kuriyan@berkeley.edu
[5]These authors contributed equally to this work.
[6]Present address: Merck Research Laboratories, P.O. Box 2000, RY50-105, Rahway, New Jersey 07065.

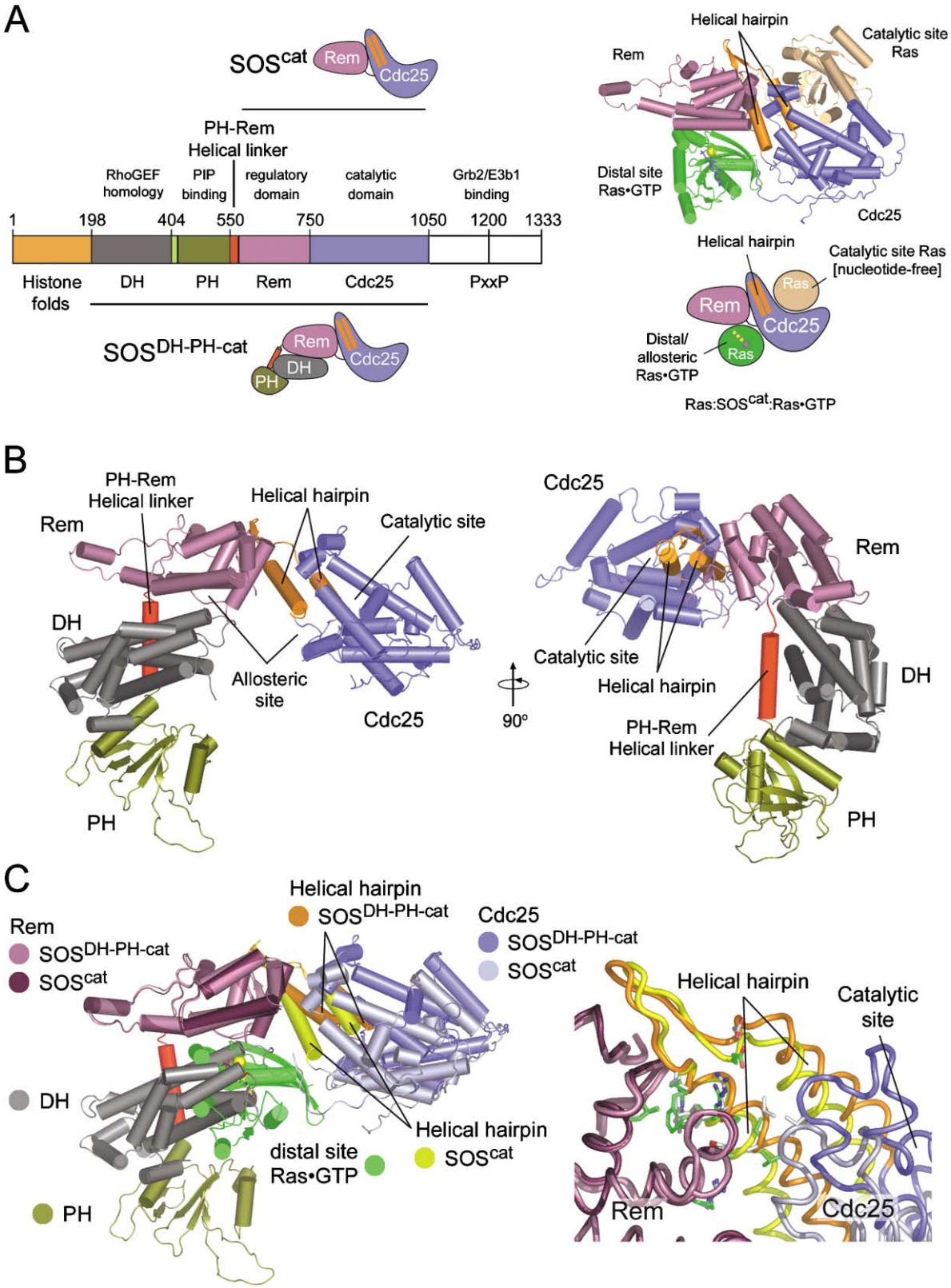

Figure 1. Structure of SOS$^{DH-PH-cat}$

(A) Domain organization of SOS and overview of a ternary Ras:SOS complex. The crystal structure of the Ras:SOS^{cat}:Ras^{Y64A}•GppNp ternary complex is shown (Margarit et al., 2003; PDB code 1NVV). The helical hairpin of the Cdc25 domain is shown in orange.

(B) The crystal structure of SOS$^{DH-PH-cat}$. Two orthogonal views are shown with coloring according to the diagram shown in (A).

(C) Comparison of SOS$^{DH-PH-cat}$ with the structure of the ternary Ras:SOS^{cat}:Ras•GTP complex (PDB code 1NVV). The structures were aligned through superpositioning of the two respective Rem domains of SOS$^{DH-PH-cat}$ and SOS^{cat}. Ras at the catalytic site is not shown for clarity (see [A]). Note that the distal Ras^{Y64A}•GppNp (green) in the ternary complex overlaps with the DH domain of SOS$^{DH-PH-cat}$. A close-up view of the Rem-Cdc25 interface is shown (right).

of $SOS^{DH\text{-}PH\text{-}cat}$, we show that the DH-PH unit inhibits SOS by blocking the distal allosteric Ras•GTP binding site of SOS. Surprisingly, blockage of the allosteric Ras binding site suppresses both the unstimulated (by Ras•GTP) and the allosterically stimulated levels of activity of SOS, leading to the discovery that the basal level of SOS activity is dependent on the binding of Ras•GDP to the distal site. It appears that the SOS protein has evolved to have its nucleotide exchange activity be masked until as yet undiscovered signals trigger the displacement of the DH-PH unit and the opening of the allosteric site, allowing Ras itself to stimulate SOS to first low and then high levels of activity.

Results and Discussion

Crystal Structure of $SOS^{DH\text{-}PH\text{-}cat}$

We determined the crystal structure of $SOS^{DH\text{-}PH\text{-}cat}$ at 3.62 Å resolution using phases determined experimentally to 4.0 Å resolution (see Experimental Procedures and Supplemental Tables S1 and S2 at http://www.cell.com/cgi/content/full/119/3/393/DC1/). Extensive screening of crystallization conditions did not improve crystalline order, and, given the resolution of the X-ray data, we have chosen not to refine individual atomic positions. Instead, we limited model optimization to rigid-body refinement of the positions and orientations of the individual domains, which are placed with high confidence because of the excellent quality of the experimental electron density maps (see Supplemental Figure S1). These maps suggest that the structure of each domain is essentially the same as that seen previously in crystal structures of the isolated DH-PH module and the SOS^{cat} domain bound to Ras (Soisson et al., 1998; Boriack-Sjodin et al., 1998; Margarit et al., 2003).

The crystals contain two molecules of $SOS^{DH\text{-}PH\text{-}cat}$ in the asymmetric unit, with similar structure. $SOS^{DH\text{-}PH\text{-}cat}$ forms a curved C-shaped assembly that has the PH domain at one end and the Cdc25 domain at the other (Figure 1B). The PH domain interacts only with the DH domain, which in turn packs against the face of the Rem domain that is distal to the Cdc25 domain and makes no contact with the latter. A helical linker (residues 550–566) that is not present in previous models is seen to connect the PH and Rem domains and was traced unambiguously (Figure 1 and see Supplemental Figure S1 on the *Cell* web site). This linker packs against a hydrophobic patch on the DH domain, with ~1500 $Å^2$ of surface area buried at the interface, and may therefore be important in positioning the DH-PH module with respect to SOS^{cat} (Figure 1B). The internal structure of the DH-PH unit within this assembly is essentially the same as that seen previously in the structure of the isolated DH-PH domains (Soisson et al., 1998).

The general structure of the SOS^{cat} module in $SOS^{DH\text{-}PH\text{-}cat}$ is distorted slightly with respect to that seen previously in binary or ternary complexes of SOS bound to Ras (Boriack-Sjodin et al., 1998; Margarit et al., 2003) (Figure 1C). In the two molecules in the asymmetric unit of the crystal, the Rem and Cdc25 domains are splayed apart by 20° and 28°, respectively, so that the tight contact between the Rem domain and the helical hairpin structure of the Cdc25 domain, seen in crystal structures of SOS^{cat} bound to Ras, is broken in $SOS^{DH\text{-}PH\text{-}cat}$ (Figure 1C). The interface between the Rem domain and the helical hairpin of the Cdc25 domain is known to be important for SOS activity (Hall et al., 2001), and the disruption of this interface correlates with the reduced level of nucleotide exchange activity exhibited by $SOS^{DH\text{-}PH\text{-}cat}$ (see below).

A notable feature of the $SOS^{DH\text{-}PH\text{-}cat}$ structure is the location of the DH domain, which is positioned so that it blocks the allosteric binding site for Ras (Figure 1C). This feature predicts that the nucleotide exchange activity of $SOS^{DH\text{-}PH\text{-}cat}$ would not be readily stimulated by Ras•GTP, since the binding of Ras•GTP to the distal site would require that the DH domain swing out of the way.

The DH domain packs against the Rem domain, with an interface that is conserved in sequence from humans (SOS1 and SOS2) to *C. elegans*, and is composed mainly of polar residues (Figure 2A). There are differences in the relative positioning of the DH and Rem domains in the two molecules in the asymmetric unit, in which the DH domains are rotated by 11° with respect to one another (data not shown). Despite the loose nature of its linkage to the Rem domain, the DH domain appears to act as an efficient latch on the distal Ras binding site of SOS because of its stable positioning by the helical PH-Rem linker (Figures 1B and 1C).

The DH-PH Unit Inhibits the Ras-Specific Nucleotide Exchange Activity of SOS

In assaying the nucleotide exchange activity of $SOS^{DH\text{-}PH\text{-}cat}$, we take advantage of a mutant form of Ras, Ras^{Y64A}, which binds to the distal site of SOS but not to the catalytic site (Margarit et al., 2003; Hall et al., 2001; Boriack-Sjodin et al., 1998). We also discuss two mutant forms of SOS. $SOS^{cat:W729E}$ does not bind Ras at the distal site (Figure 2B) (see below), and $SOS^{DH\text{-}PH\text{-}cat:triple.mut}$ (E268A/M269A/D271A) has a weakened Rem-DH interface (Figure 2A). These two mutant forms of SOS are part of a large set of mutations that we have screened for activity, and, since our results are internally consistent, we focus mainly on these two for clarity. In experiments that call for Ras•GTP, we use the nonhydrolysable GTP analog GppNp instead of GTP, so that the hydrolysis of GTP by Ras is not a complicating factor. For simplicity, we refer to Ras•GppNp as "Ras•GTP."

The autoinhibition of $SOS^{DH\text{-}PH\text{-}cat}$ is demonstrated by an assay in which the release of fluorescently labeled GDP from Ras is monitored (Ahmadian et al., 2002) (Figure 2C). When the SOS:Ras•GDP ratio is 1:1, the release of GDP from Ras is about three times slower with $SOS^{DH\text{-}PH\text{-}cat}$ when compared to SOS^{cat} (Figures 2C and 2F). More strikingly, $SOS^{DH\text{-}PH\text{-}cat}$ is inert to allosteric stimulation by Ras•GTP. Whereas addition of stoichiometric amounts of Ras^{Y64A}•GTP accelerates the turnover by SOS^{cat} significantly, there is no significant increase in the rate of the $SOS^{DH\text{-}PH\text{-}cat}$-catalyzed nucleotide release under identical conditions (Figure 2). The addition of a 20-fold molar excess of Ras^{Y64A}•GTP to $SOS^{DH\text{-}PH\text{-}cat}$ increases the rate of GDP release from Ras only marginally, to a level comparable of that obtained with the SOS^{cat} domain in the absence of Ras^{Y64A}•GTP (Figure 2C).

The inability of Ras•GTP to stimulate the activity of

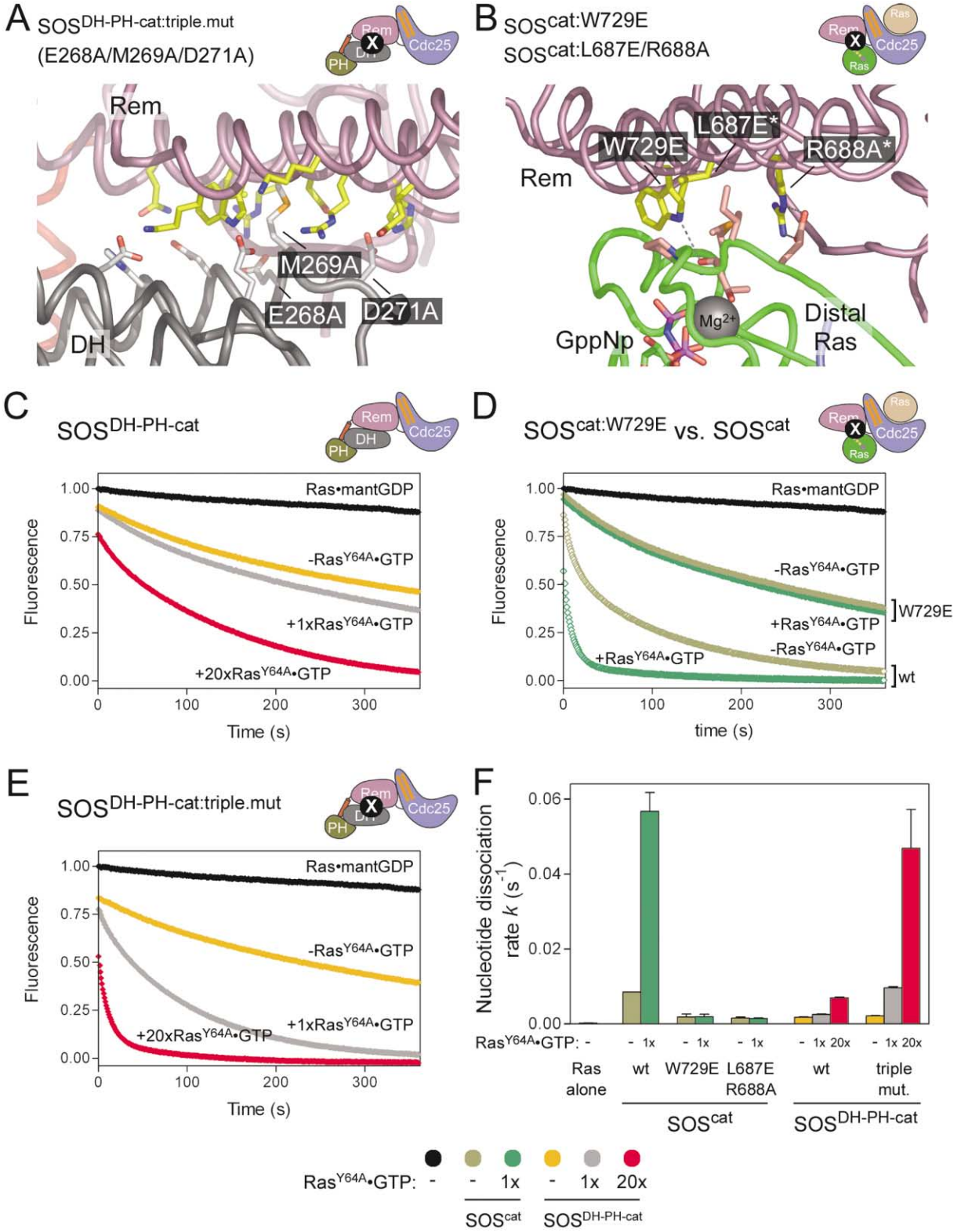

Figure 2. Kinetic Analysis of SOS$^{DH-PH-cat}$ and Mutant Forms of SOS^{cat} and SOS$^{DH-PH-cat}$

(A) Interactions between the DH and Rem domains in SOS$^{DH-PH-cat}$. The combination of mutations analyzed in (E) and (F) and in Figure 5 are shown.

(B) Interactions between the Rem domain of SOS and Ras at the distal binding site on SOS. The structure of a ternary Ras:SOS^{cat}:Ras•GTP complex is shown (PDB code 1NVV; Margarit et al., 2003). Mutations analyzed in (D) and (F) and Figures 3 and 5 are shown. Asterisks indicate double mutants.

(C) Nucleotide exchange rates for SOS$^{DH-PH-cat}$. Ras•mantGDP (1 μM) was incubated in buffer containing unlabeled GDP (200 μM) in the absence

$SOS^{DH\text{-}PH\text{-}cat}$ is consistent with the crystal structure, in which the DH domain blocks the allosteric binding site for Ras. This naturally raises the question as to the nature of the trigger that releases this inhibition. This issue is unresolved at present, but mutations at the DH-Rem interface that are expected to destabilize the interaction between the DH and Rem domains (Figure 2A; $SOS^{DH\text{-}PH\text{-}cat:triple.mut}$) have the effect of partially relieving the inhibitory effect of the DH domain on the stimulation of $SOS^{DH\text{-}PH\text{-}cat}$ by Ras•GTP (Figures 2E and 2F; a cell-based assay of this mutant is discussed in a later section). Although the basal activity of $SOS^{DH\text{-}PH\text{-}cat:triple.mut}$ is not increased significantly compared to wild-type (Figures 2C and 2E), the mutant protein is more readily stimulated by the addition of Ras•GTP. Addition of Ras^{Y64A}•GTP, in a stoichiometry of 1:1 relative to $SOS^{DH\text{-}PH\text{-}cat:triple.mut}$, yields nucleotide exchange rates that are comparable to those of the isolated, unstimulated SOS^{cat} domain, and a 20-fold molar excess of Ras^{Y64A}•GTP increases the rate to the maximal level observed when SOS^{cat} is stimulated by Ras•GTP (Figures 2E and 2F).

Blockage of the Distal Ras Binding Site Decreases the Affinity of SOS for Ras at the Catalytic Site

To further assess the autoinhibition of SOS experimentally, we measured the affinity of Ras for the catalytic site of SOS by using fluorescence anisotropy. In these experiments, we use Oregon green-labeled Ras (see Experimental Procedures) that can, in principle, bind to either the active site of SOS or the distal site. The experiments are set up so that the distal site is either blocked, as in $SOS^{DH\text{-}PH\text{-}cat}$ or SOS^{cat}:Ras^{Y64A}•GTP, or disrupted by mutation, as in $SOS^{cat:W729E}$ (see below) (Figures 3 and 5). Our analysis is thus interpreted in terms of the binding of Ras at the catalytic site.

It is intriguing that the presence of the DH-PH unit in $SOS^{DH\text{-}PH\text{-}cat}$ not only blocks the binding of the allosteric Ras•GTP, as is expected from the crystal structure, but also reduces the affinity of the catalytic site for Ras (Figure 3). Similar results are obtained for $SOS^{cat:W729E}$, which does not bind Ras at the distal site. From the titration curves, we estimate that Ras has relatively low affinity for the catalytic sites of $SOS^{DH\text{-}PH\text{-}cat}$ and the SOS mutant that cannot bind the distal Ras ($SOS^{cat:W729E}$) (K_d ~29.9 μM and ~14.5 μM, respectively) (Figure 3). In contrast, when we load the distal site of SOS^{cat} with Ras^{Y64A}•GTP, added in 10-fold molar excess to saturate the distal site, the affinity for Ras at the catalytic site is significantly higher (K_d ~1.9 μM). The ability of Ras bound to the distal site to increase the affinity of Ras for the catalytic site of SOS is likely to be a key component of the mechanism by which Ras stimulates the activity of SOS.

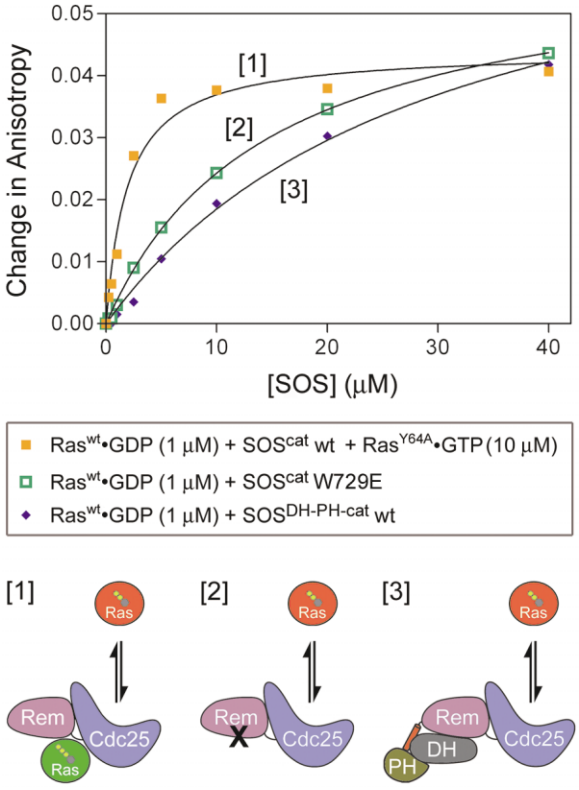

Figure 3. Binding of Ras to the Catalytic Site of SOS

$Ras^{C118S/A122C}$ was labeled with Oregon green and loaded with GDP. Fluorescence anisotropy was used to measure the affinity of $Ras^{C118S/A122C}$•GDP (1 μM) for the catalytic site of $SOS^{cat:W729E}$, SOS^{cat}:Ras^{Y64A}•GppNp (10 μM), and $SOS^{DH\text{-}PH\text{-}cat}$. The fluorescence anisotropy of $Ras^{C118S/A122C}$•GDP alone was subtracted from each data point of the titration. Affinities were estimated by nonlinear regression (K_d, Ras•GDP:$SOS^{cat:Mut.W729E}$ ~14.5 μM; K_d, Ras•GDP:SOS^{cat}:Ras^{Y64A}•GppNp ~1.9 μM; K_d, Ras •GDP: $SOS^{DH\text{-}PH\text{-}cat}$ ~29.9 μM).

Crystal Structure of a Ras:SOS^{cat}:Ras^{Y64A}•GDP Complex

The structure of $SOS^{DH\text{-}PH\text{-}cat}$ explains the inability of Ras•GTP to stimulate nucleotide exchange activity robustly, since the distal binding site is blocked. The structure does not provide a ready explanation for our observation that the basal level of activity displayed by $SOS^{DH\text{-}PH\text{-}cat}$ (i.e., unstimulated by Ras•GTP) is lower than

or presence of $SOS^{DH\text{-}PH\text{-}cat}$ (1 μM). The release of labeled nucleotide in the presence of stoichiometric amounts of Ras^{Y64A}•GppNp (1× and 20×) is shown.

(D) Comparison of SOS^{cat}- and $SOS^{cat:W729E}$-mediated nucleotide release. The assay conditions are identical to (C), except that the wild-type and the mutant form of SOS^{Cat} (see [B]) were used.

(E) Nucleotide exchange by $SOS^{DH\text{-}PH\text{-}cat}$ with mutations in the DH:Rem domain interface. The assay conditions are identical to (C), except that the mutant form of $SOS^{DH\text{-}PH\text{-}Cat}$, $SOS^{DH\text{-}PH\text{-}cat:triple.mut}$ (see [A]), was used.

(F) Comparison of nucleotide exchange rates of wild-type and mutant forms of $SOS^{DH\text{-}PH\text{-}cat}$ and SOS^{cat}. Rates were fitted to single exponentials. Error bars indicate standard deviations of three independent experiments. Colors are consistent with (C), (D), and (E). Orange bars represent the basal, unstimulated $SOS^{DH\text{-}PH\text{-}cat}$-mediated exchange rate; gray and red bars show rates in presence of 1 μM and 20 μM Ras^{Y64A}•GTP, respectively. SOS^{cat}-catalyzed exchange rates in the absence and presence of Ras^{Y64A}•GTP are shown in olive and green, respectively. Nucleotide exchange rates for wild-type SOS^{cat} and two mutant variants, $SOS^{cat:W729E}$ and $SOS^{cat:L687E/R688A}$ (see [B]), are shown.

that for SOS^{cat} in the absence of Ras•GTP (Figures 2C and 2F). The DH domain in $SOS^{DH\text{-}PH\text{-}cat}$ makes no contact with the Cdc25 domain, and electron density maps reveal no evidence for significant structural changes within the Rem or Cdc25 domains of $SOS^{DH\text{-}PH\text{-}cat}$, thus ruling out any obvious mechanism for the transmission of conformational changes that might couple DH-Rem interactions to changes at the Cdc25 active site.

It occurred to us that the most ready explanation for the observed breakage of the Rem-Cdc25 interactions in $SOS^{DH\text{-}PH\text{-}cat}$ is that this interface might be intrinsically unstable in the absence of Ras bound at the distal binding site (Figure 1C). We have shown previously that Ras•GTP binding to the distal site brings these two domains of SOS^{cat} closer together, thereby stabilizing the helical hairpin of the Cdc25 domain, a structural element that is critical for Ras binding at the active site (Margarit et al., 2003). In this section, we present a crystal structure of a ternary complex of Ras:SOS^{cat}:Ras^{Y64A}•GDP. This structure demonstrates that Ras•GDP can also provide the bridging function at the distal site, suggesting that the decreased nucleotide exchange levels of $SOS^{DH\text{-}PH\text{-}cat}$ and $SOS^{cat:W729E}$ are due to lack of Ras binding at the distal site.

Crystals of the ternary Ras:SOS^{cat}:Ras•GTP complexes that we have reported on earlier were obtained by purifying these complexes by gel filtration chromatography. Ras^{Y64A}•GDP binds to SOS^{cat} with too low an affinity for the isolation of ternary complexes by gel filtration chromatography. Instead, we obtained crystals of such a complex by adding a 4-fold molar excess of Ras^{Y64A}•GDP to a binary Ras:SOS^{cat} complex and setting up crystallization trials with these solutions. Crystals were obtained under conditions that are similar to those described previously for the Ras:SOS^{cat}:Ras•GTP complexes (see Experimental Procedures; Margarit et al., 2003). Diffraction data to 2.7 Å resolution were collected using synchrotron radiation, and structure determination was straightforward because the space group and unit cell dimensions (space group I422, $a = b = 183.7$ Å, $c = 177.8$ Å, one complex in the asymmetric unit) are similar to those of the ternary Ras•GTP complex.

The structure of the Ras:SOS^{cat}:Ras^{Y64A}•GDP complex closely resembles that of the ternary Ras:SOS^{cat}:Ras•GTP complexes determined previously, except that the nucleotide binding site of the distal (allosteric) Ras is occupied by GDP and a phosphate ion (P_i), instead of GTP (Figure 4A). Difference electron density maps reveal a break in electron density between the β-phosphate of the bound nucleotide and the phosphate ion (Figure 4A). The distance between the β-phosphate of GDP and the phosphate ion (4.1 Å) is significantly larger than that between the β- and γ-phosphates of the nucleotide in Ras•GTP and Ras•GppNp (~3 Å) (Figures 4A and 4B). Furthermore, refinement with GTP instead of GDP modeled at the Ras active site results in strong negative electron density across the terminal phosphate bond and strong positive density for a dissociated phosphate ion, consistent with the nucleotide bound state being GDP•P_i•Mg^{2+} (Figure 4C).

Ras•GDP•P_i bound at the distal site of SOS adopts a conformation that is characteristic of Ras•GTP, confirming that the distal site has primary specificity for Ras•GTP (Figures 4D and 4E) (Pai et al., 1990; Milburn et al., 1990). The coordination of empty Ras at the catalytic site of SOS is identical in both ternary complexes, with either Ras•GTP or Ras•GDP•P_i bound at the distal site, demonstrating that the binding of Ras•GDP at the allosteric site accomplishes the same structural effects at the active site of SOS^{cat} as does the binding of Ras•GTP. The phosphate ion concentration in the crystallization condition is 1.2 M, which might account for the presence of free phosphate at the nucleotide binding site. Binding measurements carried out in the absence of added phosphate ion (see below) demonstrate that this is not a requirement for Ras•GDP binding to the distal site.

Significant differences between the structures of Ras•GTP and Ras•GDP•P_i bound to the distal site are localized mainly to the switch 2 region (Figure 4D), with switch 1 of Ras•GDP•P_i being essentially in the conformation seen previously for Ras•GTP complexes. Gln-61 in switch 2 is pushed outwards by the phosphate ion, and the switch region adjusts accordingly. The coordination of GDP•P_i in Ras is similar to that seen in Arl2, another GTPase whose structure has been solved with GDP•P_i•Mg^{2+} bound at the active site (Hanzal-Bayer et al., 2002). The Arl2 structure was determined in complex with an effector protein, phosphodiesterase δ, the presence of which may stabilize the GTP bound conformation of the switch regions even in the presence of GDP•P_i.

Affinity of Ras for the Distal/Allosteric Site on SOS

We determined the affinity of Ras^{Y64A} for the distal site in SOS by fluorescence anisotropy measurements using an Oregon green-labeled mutant variant of Ras^{Y64A} (see Experimental Procedures). The change in fluorescence anisotropy upon addition of SOS reflects the formation of a Ras:SOS complex in solution (Figure 5A). The affinity of SOS^{cat} for Ras^{Y64A}•GTP at the distal site is relatively high (K_d ~3.6 μM). Ras^{Y64A}•GDP shows weaker binding (K_d ~24.5 μM) (Figure 5A). This is consistent with nucleotide exchange assays, in which an ~10-fold excess of Ras^{Y64A}•GDP over SOS^{cat} provides the same stimulation as a 1:1 ratio of Ras^{Y64A}•GTP and SOS^{cat} (Supplemental Figure S2).

As a control, the titrations were repeated with $SOS^{cat:W729E}$, the mutant form of SOS that is not expected to bind Ras at the distal site because of the critical role of Trp-729 in coordinating Ras residues (Figure 2B). No significant change in fluorescence anisotropy was observed during the titration for Ras^{Y64A} loaded with GDP or GTP, indicating that the change in fluorescence anisotropy observed with wild-type SOS^{cat} corresponds to Ras binding at the distal site (Figures 5A and 5B).

To compare the binding of Ras at the distal site in wild-type and mutant forms of $SOS^{DH\text{-}PH\text{-}cat}$, we measured the fluorescence anisotropy using a concentration of SOS and Ras such that binding of SOS^{cat} to Ras^{Y64A}•GTP is almost maximal and binding of Ras^{Y64A}•GDP is clearly detectable (see arrow in Figure 5A). Titrations for Ras^{Y64A}•GTP binding to $SOS^{DH\text{-}PH\text{-}cat}$ and a mutant form, $SOS^{DH\text{-}PH\text{-}cat:triple.mut}$ (E268A/M269A/D271A, Figure 2A), are shown as Supplemental Data (Supplemental Figure

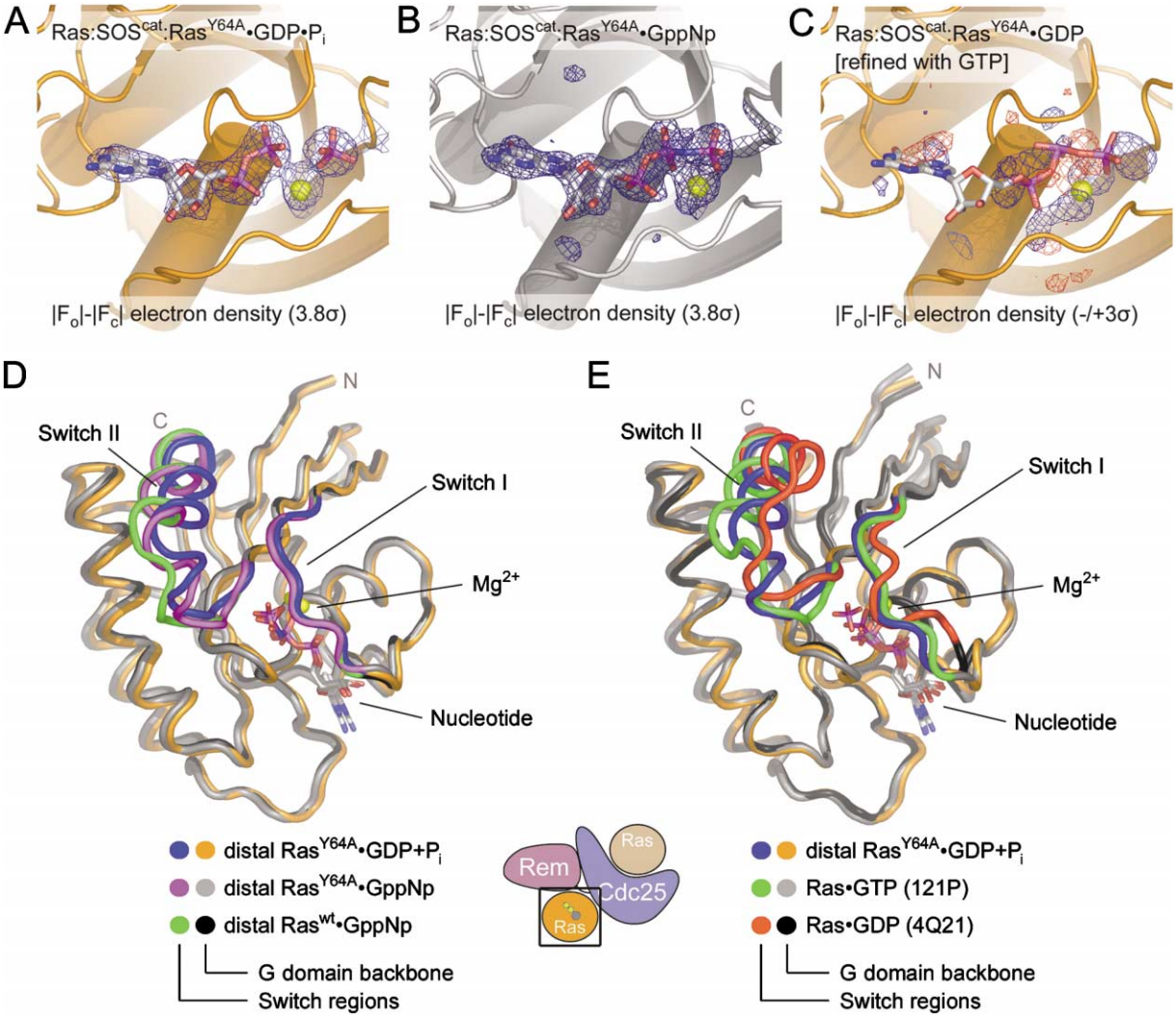

Figure 4. Structure of a Ras:SOS^{cat}:Ras^{Y64A}•GDP Complex

(A) Distal Ras^{Y64A}•GDP•P$_i$ in the structure of the ternary complex. The electron density map shown has amplitudes of (|F$_o$| − |F$_c$|), with F$_o$ and F$_c$ being the observed and calculated structure factors. Phases were calculated from a model at a stage of the refinement prior to inclusion of nucleotide. The blue electron density contour is at 3.8σ. Mg^{2+} is shown as a yellow sphere.

(B) Distal Ras^{Y64A}•GppNp in the structure of the ternary Ras:SOS^{cat}:Ras^{Y64A}•GppNp complex (Margarit et al., 2003). The electron density map shown was calculated as in (A), with phases calculated from a model of the Ras:SOS^{cat}:Ras^{Y64A}•GppNp complex (PDB code 1NVV) at a stage of the refinement prior to inclusion of nucleotide. The electron density contour is at 3.8σ.

(C) Distal Ras in the ternary Ras:SOS^{cat}:Ras^{Y64A}•GDP•P$_i$ complex, refined with GTP instead of GDP bound to Ras. In this case, the phases used to calculate the electron density map were derived from a model that included GTP, with (|F$_o$| − |F$_c$|) amplitudes. Positive density is shown in blue, and negative density is shown in red. The electron densities are contoured at 3σ and −3σ, respectively.

(D) Comparison of distal Ras conformations in Ras:SOS^{cat}:Ras•GXP complexes. Distal Ras•GppNp from structures of ternary complexes (PDB codes 1NVV [gray] and 1NVW [black]) were superimposed on Ras^{Y64A}•GDP•P$_i$ (orange) from the ternary complex. Switch 1 and 2 regions are highlighted (blue, Ras^{Y64A}•GDP•P$_i$; magenta, Ras^{Y64A}•GppNp; green, Ras^{wt}•GppNp).

(E) Comparison of distal Ras in the Ras:SOS^{cat}:Ras^{Y64A}•GDP•P$_i$ complexes with conformations of free Ras. Distal Ras^{Y64A}•GDP•P$_i$ from the ternary complex structure was superimposed on Ras•GTP (PDB code 121P) and Ras•GDP (PDB code 4Q21). Switch 1 and 2 regions are highlighted (blue, Ras^{Y64A}•GDP•P$_i$; red, Ras^{wt}•GDP; green, Ras^{wt}•GTP).

S3A). SOS$^{DH-PH-cat}$ does not bind Ras^{Y64A}•GTP to a significant level, consistent with results reported above (Figures 2C and 5B). A mutant form of SOS$^{DH-PH-cat}$ (SOS$^{DH-PH-cat:triple.mut}$; E268A/M269A/D271A, Figure 2A), in which the Rem-DH interface is weakened by replacing three interfacial residues by alanine (Figure 2A), shows detectable binding of Ras^{Y64A}•GTP (Figure 5B) and, to a lesser extent, Ras^{Y64A}•GDP (Supplemental Figure S3B). This mutant form of SOS$^{DH-PH-cat}$ also shows significant activation by allosteric Ras^{Y64A}•GTP (Figures 2E and 2F).

Mutations in SOS^{cat} that Block Distal Ras Binding Mimic the Autoinhibited State of SOS$^{DH-PH-cat}$

Taken together, our results suggest that a primary role of the DH domain in the autoinhibitory mechanism is to block the binding of Ras•GDP and Ras•GTP to the distal

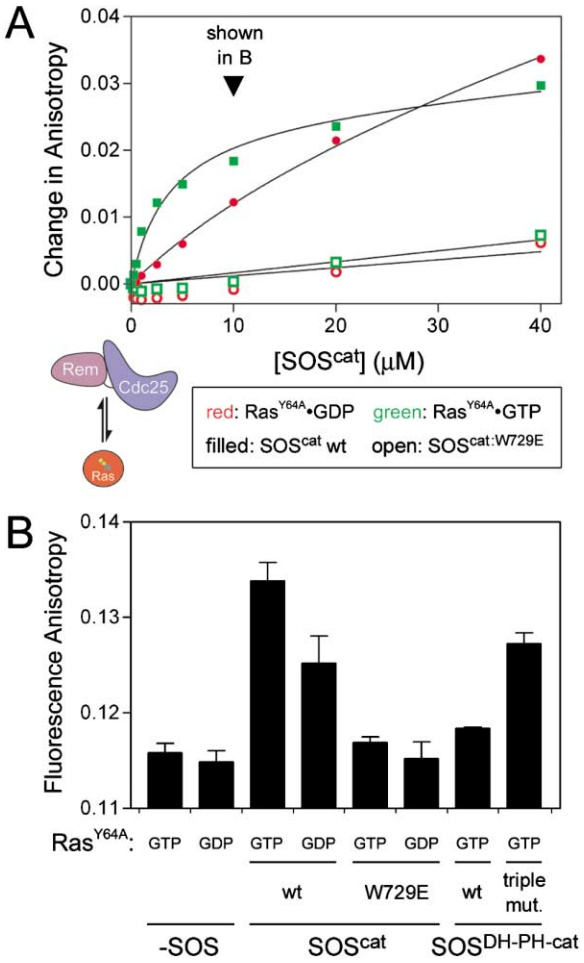

Figure 5. Binding of Ras to the Distal Site of SOS

(A) Binding of Ras^{Y64A} to the distal binding sites of SOS. Binding of Oregon green-labeled $Ras^{Y64A/C118S/A122C}$ to SOS^{cat} was monitored by changes in fluorescence anisotropy. $Ras^{Y64A/C118S/A122C}$ (1 μM) was loaded with GppNp (green) or GDP (red). Increasing amounts of wild-type SOS^{cat} (filled symbols) or $SOS^{cat:W729E}$ (open symbols) were added. The fluorescence anisotropy of $Ras^{Y64A/C118S/A122C}$ alone was subtracted from each data point of the titration. Affinities were estimated by nonlinear regression (K_d, Ras^{Y64A}•GppNp:SOS^{cat} ~3.6 μM; K_d, Ras^{Y64A}•GppNp:SOS^{cat} ~24.5 μM; no binding to $SOS^{cat:W729E}$).

(B) Ras^{Y64A} binding to SOS^{cat} and $SOS^{DH-PH-cat}$. Fluorescence anisotropy of labeled $Ras^{Y64A/C118S/A122C}$ (1 μM) was measured in the absence and presence of wild-type SOS^{cat}, $SOS^{cat:W729E}$, wild-type $SOS^{DH-PH-cat}$, or $SOS^{DH-PH-cat:triple.mut}$ (10 μM). For mutant forms of SOS^{cat} and $SOS^{DH-PH-cat}$ variants, only $Ras^{Y64A/C118S/A122C}$•GppNp binding is shown, since GDP-loaded Ras is expected to show weaker binding based on the results described in (A).

site, rather than to directly induce structural changes in the catalytic site of SOS. This is consistent with the effects of mutations in SOS^{cat} that disrupt the binding site for distal Ras. In nucleotide exchange assays, $SOS^{cat:W729E}$ has lower basal activity than wild-type SOS^{cat}, and the allosteric stimulation by Ras•GTP is lost, as is the case for $SOS^{DH-PH-cat}$ (Figures 2D and 2F). We also generated another mutant form of SOS^{cat}, in which Arg-688 and Leu-687 are replaced by alanine and glutamic acid, respectively ($SOS^{cat:L687E/R688A}$). Like Trp-729, these two residues are located at the base of the Rem domain and interact with the switch 1 region of Ras•GTP or Ras•GDP bound at the distal site (Figure 2B). As seen for $SOS^{cat:W729E}$, $SOS^{cat:L687E/R688A}$ has lower basal exchange activity than wild-type SOS^{cat} and is not stimulated by Ras•GTP (Figure 2F). These results point to the importance of Ras•GDP in enabling an intermediate activity of SOS, a fact that was not appreciated previously because Ras•GDP was always present in the assay solutions used to measure SOS activity.

Importance of the Allosteric Binding Site for the Activation of Ras in Cellular Assays

To further validate the relevance of the allosteric mechanism of SOS, we turned to a cell-based assay for SOS activity. COS1 cells were cotransfected with expression plasmids encoding T7-tagged SOS constructs and a vector from which HA-tagged ERK2 is expressed, as described earlier (Corbalan-Garcia et al., 1998). Transfection efficiencies were adjusted to yield similar levels of expression of the various SOS constructs. ERK2 was immunoprecipitated with anti-HA antibodies, and its kinase activity was assayed using myelin basic protein (MBP) as a generic substrate.

Expression of SOS^{cat} in cells leads to robust activation of ERK2, as seen previously (Figure 6 and Corbalan-Garcia et al. [1998]). Consistent with the results described above, the two mutant SOS^{cat} proteins that block allosteric Ras binding in vitro ($SOS^{cat:W729E}$ and $SOS^{cat:L687E/R688A}$) are significantly impaired in their ability to stimulate ERK2 kinase activity (Figure 6A). These results provide evidence for the importance of the allosteric site of SOS for the activation of Ras in a cellular context.

Previous experiments have shown that the entire N-terminal segment of SOS, including the histone folds in addition to the DH-PH unit, inhibits SOS activity in cells (Corbalan-Garcia et al., 1998). We now show that the DH domain is the critical element of this autoinhibition. Whereas expression of constructs containing the DH domain ($SOS^{H-DH-PH-cat}$ and $SOS^{DH-PH-cat}$) result in significantly reduced stimulation of ERK2 kinase activity (Figure 6B and Corbalan-Garcia et al. [1998]), constructs lacking the DH domain, either by N-terminal or internal deletion (SOS^{PH-cat} or $SOS^{\Delta DH}$), show levels of ERK2 activation similar to SOS^{cat}. The differences between panels A and B (Figure 6) with respect to the extent of ERK2 activation by SOS^{cat} reflect differences in SOS^{cat} expression levels due to experimental variations in transfection efficiencies. Mutations at the DH-Rem interface ($SOS^{DH-PH-cat:triple.mut}$ and another mutant form of $SOS^{DH-PH-cat}$ with additional mutations) partially alleviate the autoinhibition in the cell-based assay, again consistent with our in vitro data (Supplemental Figure S4).

Conclusions

The activation of Ras has profound consequences for the cell, with downstream effects ranging from alterations in cellular architecture and motility to changes in the control of cell cycle and differentiation programs (Coleman et al., 2004). Given the ability of activated Ras to so potently affect cellular function, it is perhaps to be expected that the Ras activator SOS is subject to complex regulatory control. What is surprising in our

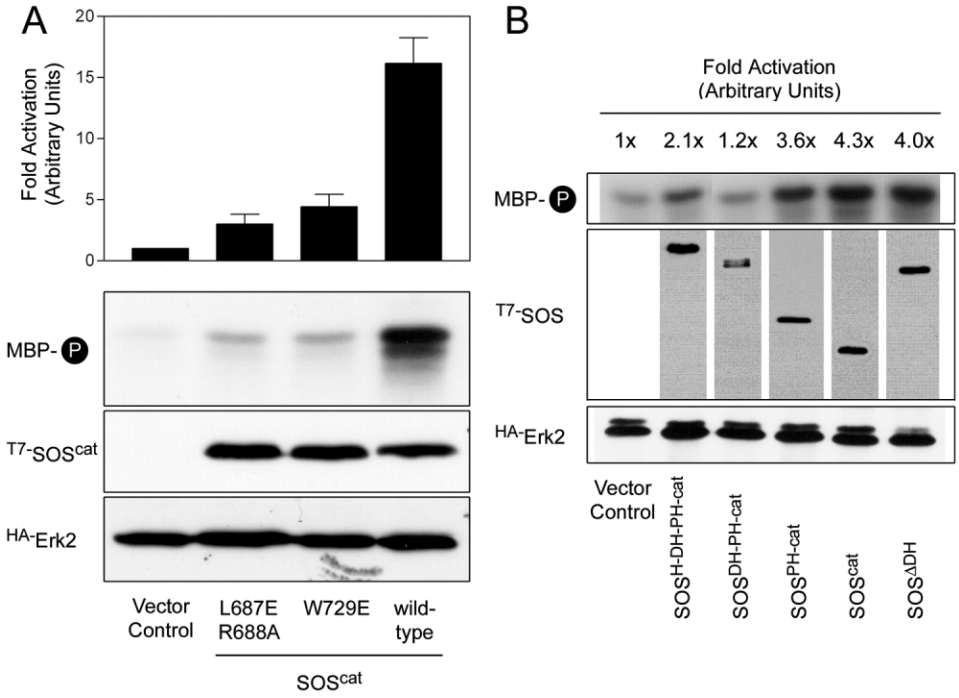

Figure 6. Activation of ERK MAP Kinase by SOS

COS1 cells were transiently cotransfected with HA-tagged ERK2 and T7-tagged SOS constructs as indicated. ERK2 activation was measured in serum-starved cells by an immunoprecipitated kinase-kinase assay using myelin basic protein (MBP) as a substrate. Results were normalized to the vector control reaction. Western blots detecting T7- and HA-tagged proteins are shown. (A) Activation of ERK2 by SOS^{cat} and SOS^{cat} mutants. Results shown in the bar diagram are from three independent experiments. Error bars indicate standard deviations of three independent experiments. The amout of ^{32}P incorporation into MBP was quantified by phosphorimaging. Autoradiograms and Western blots shown are from a single representative experiment. (B) Activation of ERK2 by SOS truncations. Results shown are from a single representative experiment. Experiments were repeated three times with similar results.

findings is the central role for Ras itself in determining the activation status of SOS. We had shown previously that Ras•GTP stimulates SOS to maximal levels of activity (Margarit et al., 2003). Ras•GTP binds with high affinity to the Rem and Cdc25 domains, probably stabilizing an active conformation of SOS. We have now shown that Ras•GDP binds at the same allosteric site, but with lower affinity, and sets an intermediate level of SOS activity in our assays (Figure 7A).

The crystal structure of $SOS^{DH\text{-}PH\text{-}cat}$ described here reveals that the allosteric Ras binding site in SOS is blocked by the DH domain, which is located far from the active site of SOS. It appears that the DH domain has no direct inhibitory effect on the Ras-specific nucleotide exchange reaction but rather functions as a gate for Ras binding to the allosteric site.

For robust activity inside the cell, SOS would have to adopt a conformation at the membrane or in signaling complexes such that Ras has access to both the catalytic and the allosteric sites of SOS. We do not know how the inhibitory effect of the DH domain is relieved in vivo, but we expect that some sort of release mechanism will be important, since Ras•GTP binding to the distal site by itself does not seem efficient at releasing the autoinhibition mediated by the DH domain. The kinetic parameters of the reaction described here for freely diffusing proteins in solution might differ significantly when Ras:SOS complexes are tethered at the membrane. Targeting of SOS to the membrane might itself be sufficient to render the enzyme active, as has been suggested earlier (Aronheim et al. 1994), perhaps through PH domain-mediated changes in conformation. Positioning of the phosphatidyl inositol binding site of SOS close to the membrane orients the remainder of $SOS^{DH\text{-}PH\text{-}cat}$ so that both Ras binding sites of SOS are in a plane that is parallel to the membrane, indicating a conformation optimized for Ras activation and allosteric regulation (Figure 7B). Additional effectors or modifications such as phosphatidyl inositol binding by the PH domain or phosphorylation might also be involved in the activation mechanism (Sini et al., 2004; Chen et al., 1997; Das et al., 2000). The structure of the DH-PH unit, seen previously in isolation and here as part of $SOS^{DH\text{-}PH\text{-}cat}$, is in an inactive conformation (Soisson et al., 1998; Worthylake et al., 2000). One intriguing possibility is that events at the membrane that alter the disposition of the DH-PH unit within SOS might coordinately activate SOS for both Ras and Rac1 activation.

A recent study describes the discovery of novel mutant SOS alleles in *Drosophila* that affect SOS activity, indicating an intricate regulation of SOS in vivo (Silver et al., 2004). Mapping of these mutations to the structure presented here suggests that they might be disruptive for the DH-PH interface, the helical hairpin close to the Rem-Cdc25 interface, or the Rem domain close to the distal Ras binding site. It seems clear that further study

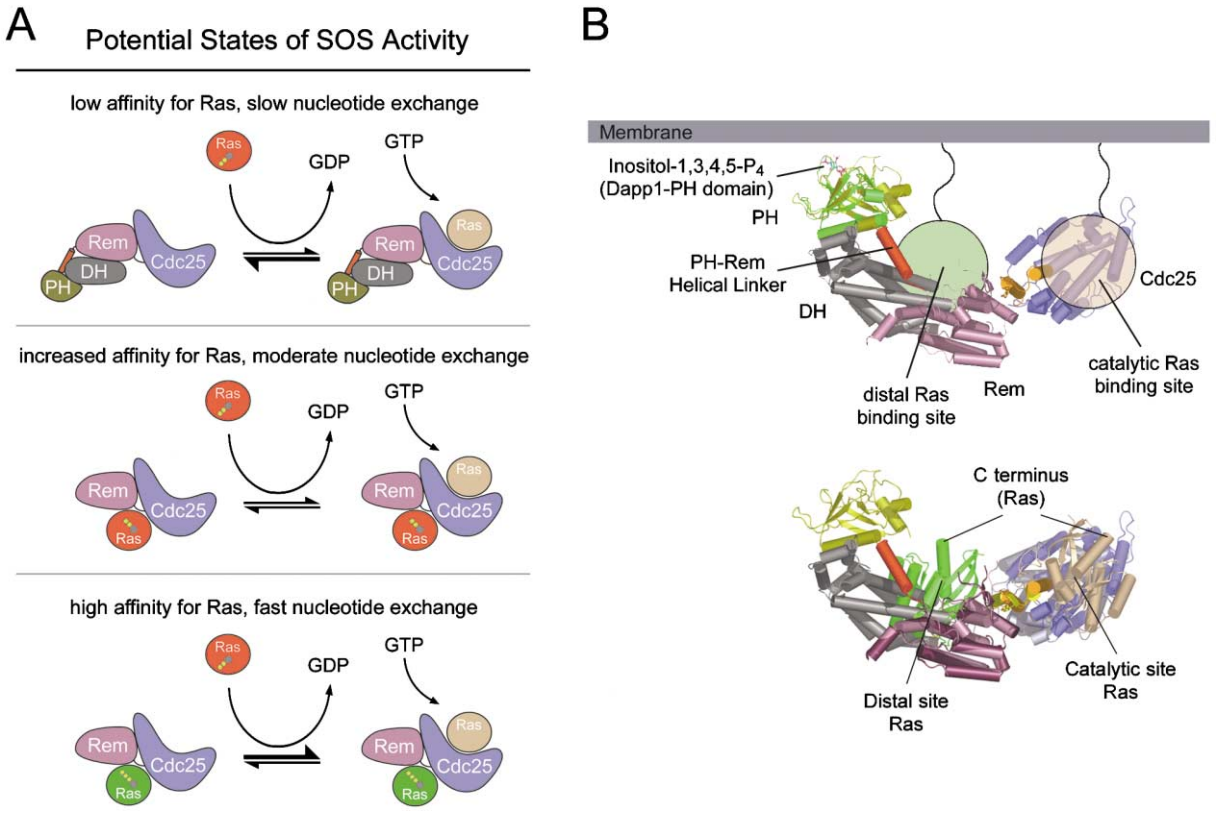

Figure 7. Models for SOS Activation

(A) Schematic diagram of potential states of SOS activity. In the autoinhibited nucleotide exchange reaction mediated by $SOS^{DH\text{-}PH\text{-}cat}$, the distal (allosteric) Ras binding site on SOS is blocked by the DH-PH unit of SOS resulting in low affinity of the catalytic site of SOS for Ras and low enzymatic activity (top). For an intermediate level of SOS activity (the SOS^{cat}-mediated nucleotide exchange), the nucleotide exchange activity of SOS is dependent on Ras•GDP binding to the distal binding site on SOS (middle). Ras•GTP binding at the distal binding site on SOS stimulates the nucleotide exchange reaction robustly (bottom).

(B) Position of the phosphatidyl inositol binding site in $SOS^{DH\text{-}PH\text{-}cat}$. The Sos PH domain was superimposed with the crystal structure of the PH domain from Dapp1 (PDB code 1FAO; Ferguson et al., 2000) in complex with Inositol-1,3,4,5-tetrakisphosphate. The membrane plane is indicated. Positioning of the phosphatidyl inositol binding site close to the membrane orients both Ras binding sites of SOS in a parallel plane with the membrane (bottom; see Figure 1C for details).

of the regulatory mechanism of SOS activity will be rewarding.

Experimental Procedures

Mutagenesis, Protein Expression, and Purification

$SOS^{DH\text{-}PH\text{-}cat}$ (residues 198–1049) and SOS^{cat} (residues 566–1049) of human SOS1 were cloned into the bacterial expression vector pProEx HTb (Invitrogen) using the NcoI/HindIII restriction sites. The vector fuses an N-terminal His_6 tag to the protein. *Escherichia coli* cells (BL21DE3, Novagen) were transformed with expression constructs and grown in Terrific Broth (TB) medium supplemented with 100 mg/ml Ampicillin. Protein production was induced by addition of 1 mM IPTG at a cell density corresponding to an absorbance of 1 at 600 nm, and the protein was expressed at 18°C for 16 hr. Cells were collected by centrifugation at 4000 × g for 1 hr, resuspended in NiNTA buffer A (25 mM Tris-Cl [pH 7.5], 500 mM NaCl, 20 mM imidazole) containing protease inhibitors, and frozen in liquid nitrogen. Cell suspensions were thawed in a water bath at 25°C and lysed by French press (EmulsiFlex-C5, Avestin). Cell debris was removed by ultracentrifugation at 100,000 × g for 1 hr at 4°C. Clear supernatants were loaded onto a NiNTA column (Qiagen) equilibrated in NiNTA buffer A. The resin was washed with 20 column volumes of the same buffer, and proteins were eluted in NiNTA buffer B (NiNTA buffer A supplemented with 500 mM imidazole). Buffers were exchanged using a Fast Desalting Column (Amersham-Pharmacia) into TEV buffer (25 mM Tris-Cl [pH 8.3], 50 mM NaCl, 5 mM β-mercaptoethanol). His_6 tags were cleaved by incubation with Tobacco etch virus (TEV) protease, and free tags and uncleaved proteins were removed by a second NiNTA column. For $SOS^{DH\text{-}PH\text{-}cat}$ and SOS^{cat}, the flowthrough was collected and loaded onto a MonoQ column (Amersham-Pharmacia) equilibrated in MonoQ buffer A (25 mM Tris-Cl [pH 8.3], 1 mM DTT). Proteins were eluted on a gradient from 0 to 500 mM NaCl over 20 column volumes. All proteins were further subjected to size exclusion chromatography on a Superdex200 column (Amersham-Pharmacia) equilibrated in gel filtration buffer (25 mM Tris-Cl [pH 7.5], 50 mM NaCl, 1 mM DTT). Fractions containing protein were pooled and concentrated on a Centricon Ultrafiltration Device (Millipore) to a final concentration of about 50 mg/ml. Protein aliquots were frozen in liquid nitrogen and stored at −80°C.

Size exclusion chromatography coupled with static multiangle light scattering measurements was used to monitor Ras:SOS complex formation and the homogeneity of purified proteins and were performed as described previously (Margarit et al., 2003; Sondermann et al., 2003).

Point mutations were introduced into the coding region of expression plasmids using the QuikChange XL Mutagenesis Kit (Stratagene) following the manufacturer's instructions. Expression and purification of mutant proteins was identical to the procedure for wild-type proteins. All mutant proteins expressed to comparable levels. Circular dichroism spectroscopy confirmed the folded state

of the mutant SOS^{cat} proteins, with spectra undistinguishable from the wild-type protein (data not shown). Mutant Ras proteins were tested for their ability to stimulate SOS by binding to the distal site ($Ras^{Y64A/C118/SA122C}$; $Ras^{C118S/A122C}$) and for their SOS-mediated nucleotide exchange reaction ($Ras^{C118S/A122C}$) and were found to be equally active as wild-type Ras (residues 1–166 of human Ha-Ras).

For crystallization of the ternary Ras^{wt}:SOS^{cat}:Ras^{Y64A}•GDP complex, a binary complex consisting of Ras^{wt} and SOS^{cat} was assembled as described earlier (Margarit et al., 2003). Ras^{Y64A} loaded with GDP was added in a 4-fold excess prior to crystallization.

Crystallization, X-Ray Data Collection, and Structure Solution

Initially, crystals were obtained for a fragment of human SOS1 that spans the DH-PH and Rem-Cdc25 domains (residues 189–1049; Figure 1A). Crystals of native and selenomethionine-substituted $SOS^{189–1049}$ were obtained by hanging drop vapor diffusion. These crystals diffract X-rays to 4.0 Å (space group $P2_12_12_1$, a = 80.5 Å, b = 125.1 Å, c = 246.2 Å, with two molecules of $SOS^{189–1049}$ in the asymmetric unit). A mercury derivative provided initial phases, which locate the positions of selenomethionines. Electron density maps calculated using experimentally determined phases to 4.3 Å, extended to 4.0 Å, were improved by B factor sharpening and by 2-fold noncrystallographic symmetry averaging.

Although at low resolution, the experimentally phased electron density maps are of high quality (Supplemental Figure S1A) and allowed each of the component domains in the two molecules to be positioned with confidence. The packing of molecules in the crystal suggested that crystallization might be improved by omitting the first nine residues of the original construct. Crystals obtained using a modified construct, $SOS^{DH-PH-cat}$ (residues 198–1049 of human SOS1), show a slight improvement in resolution, with data measured to 3.62 Å resolution. Crystals were obtained by mixing equal volumes of protein (10–50 mg/ml) and reservoir solution (10%–14% PEG200, 10% ethylene glycol, 10 mM strontium chloride, 50 mM HEPES-NaOH [pH 6.5], and 4% sucrose). Crystals appeared within 1 hr at 20°C with typical dimensions of 0.3 mm × 0.3 mm × 0.3 mm. Crystals were frozen in propane without further cryoprotection and kept at 100 K during data collection.

Crystallographic statistics for data collection are shown in Supplemental Table S1. Data sets were collected using synchrotron radiation (ALS, Berkeley, beamline 8.2.2). Data reduction was carried out with the software package HKL2000 (Otwinowski and Minor, 1997). The space group is $P2_12_12_1$ with a = 73.5 Å, b = 127.4 Å, c= 279.1 Å. The asymmetric unit consists of two molecules of $SOS^{DH-PH-cat}$, and structure determination proceeded with the initial model obtained for $SOS^{189–1049}$ for molecular replacement searches. Rigid body refinement of the individual domains of SOS using CNS (Brünger et al., 1998) yielded the final placement of the domains.

The two $SOS^{DH-PH-cat}$ molecules in the asymmetric unit interact with their Cdc25 domains in a head-to-head fashion burying 2745 $Å^2$ of solvent-accessible surface area (data not shown). Although the binding surfaces for the noncrystallographic symmetry packing of the two protomers lie across the active site of $SOS^{DH-PH-cat}$, there is no indication of dimer formation of $SOS^{DH-PH-cat}$ in solution as assayed by coupled size exclusion chromatography and multiangle light scattering measurements (data not shown).

The ternary Ras:SOS^{cat}:Ras^{Y64A}•GDP complex yielded tetragonal crystals under conditions reported previously (Margarit et al., 2003). Briefly, equal volumes of protein (20–40 mg/ml) and reservoir solution (1.2 M Na/K phosphate, 100 mM HEPES-NaOH [pH 7.5]) were mixed and incubated in hanging drops. Crystals appeared within 1 week at 4°C with dimensions of 0.03 mm × 0.02 mm × 0.02 mm. For cryoprotection, crystals were transferred to reservoir solution supplemented with 30% glycerol for 10 min, frozen in propane, and kept at 100 K during data collection.

Crystallographic statistics for data collection and refinement are shown in Supplemental Table S1. Data sets were collected using synchrotron radiation (ALS, Berkeley, beamline 8.2.1). Data reduction was carried out as previously described. The space group was determined to be I422 with similar dimensions measured for ternary Ras:SOS^{cat} complexes reported previously (a = b = 184.1 Å, c= 177.9 Å), with one complex in the asymmetric unit. The structure was refined using standard procedures and protocols using CNS starting from a previous model (PDB code 1NVV) (Brünger et al., 1998) and O (Kleywegt and Jones, 1996).

Nucleotide Exchange Assay

Nucleotide exchange assays using mantGDP were perfomed as described earlier (Ahmadian et al., 2002; Margarit et al., 2003). Briefly, purified Ras (residues 1–166 of human Ha-Ras) was incubated in a 50-fold molar excess of mantGDP, GDP, or GppNp in the presence of 4 mM EDTA in gel filtration buffer. Reactions were stopped with 10 mM $MgCl_2$, and free nucleotide was removed by gel filtration.

Nucleotide dissociation rates were measured by incubation of 1 μM Ras•mantGDP in reaction buffer (40 mM HEPES-KOH [pH 7.5], 10 mM $MgCl_2$, and 1 mM DTT) supplemented with 200 μM unlabeled GDP. When indicated, reactions were supplemented with additional proteins. The data were fitted to a single exponential decay function using the program Prism (GraphPad Software Inc.). The derived rates are qualitative because of interference by unlabeled Ras•GDP at long times and low Ras•mantGDP concentrations.

Site-Specific Labeling of Proteins with Fluorescent Probes

Fluorescent maleimide derivatives (Oregon green 488) were obtained from Molecular Probes, Inc. Protein solutions were exchanged into gel filtration buffer lacking DTT prior to labeling to remove reducing agents. Proteins (5 mg/ml) were labeled in gel filtration buffer lacking DTT for 2 hr at 25°C with a 10- to 20-fold molar excess of fluorophore. Reactions were quenched by addition of 2 mM β-mercaptoethanol, and free fluorophores were removed by gel filtration using NAP5 desalting columns. Protein concentrations were determined by standard Bradford assays. Labeling efficiency was determined by UV/VIS spectroscopy on a Cary 50 Scan spectrophotometer using the molar extinction coefficient provided by Molecular Probes, Inc. The molar ratio of fluorophore to protein typically varied between 0.6 and 0.9 moles of dye per mole of protein.

Fluorescence Anisotropy Binding Assay

For detection of binding in vitro by monitoring the change of fluorescence anisotropy upon complex formation, a mutant form of Ras was used. Cys-118 is the only cysteine residue in Ras with a surface exposed sulfhydryl group, and we mutated this residue to serine (Ras^{C118S}; Kraemer et al., 2002). Next, Ala-122, which is located within a loop region of Ras and is poorly conserved, was replaced by cysteine and labeled with the fluorescent dye Oregon green 488 maleimide.

Fluorescence anisotropy assays were performed on a Spex Jobin Yvon FluoroMax-3 fluorometer. Oregon green 488-labeled $Ras^{Y64A/C118S/A122C}$ (1 μM) or $Ras^{C118S/A122C}$ (1 μM) was incubated with increasing amounts of SOS proteins in gel filtration buffer, and the anisotropy was measured in a 500 μl quartz cuvette at excitation and emission wavelengths of 470 nm and 515 nm, respectively, with slit bandpasses set to 2 nm. Data points were taken in triplicate after 10 min of equilibration with an integration time of 20 s per measurement.

Affinities were determined by subtraction of Ras anisotropy (no SOS added). The data were fitted to saturation binding function $F_x = (x \times B_{max})/(K_d + x) - (NS \times x)$ where B_{max} is maximal binding, K_d is the dissociation constant, x is the concentration of SOS, and NS is a nonspecific binding constant) using the program Prism (GraphPad Software Inc.).

$Ras^{C118S/A122C}$ and $Ras^{Y64A/C118S/A122C}$ behave similarly to wild-type Ras and Ras^{Y64A}, respectively, in nucleotide exchange assays (data not shown).

ERK2 Immune Complex Kinase Assay

ERK2 activition was measured as described earlier (Corbalan-Garcia et al., 1998). COS1 cells, cultured in Dulbecco's modified Eagle's medium (DMEM) supplemented with 5% fetal calf serum, were transiently cotransfected with expression plasmids encoding T7-tagged SOS constructs and HA-tagged ERK2. After incubation for 24 hr in serum-free DMEM, cells were lysed in immunoprecipitation buffer (10 mM Tris-Cl [pH 7.4], 150 mM NaCl, 1% Triton X-100, 10% glyc-

erol, 1 mM EDTA, supplemented with protease inhibitors). Protein (50 μg total) from each lysate was analyzed by SDS-PAGE and Western blotting onto nitrocellulose. Immunoblot analysis of the epitope-tagged transiently expressed proteins was carried out with anti-HA and anti-T7 antibodies followed by enhanced chemiluminescence detection. ERK2 was immunoprecipitated from lysates by using anti-HA antibody. The immune complexes were washed three times with immunoprecipitation buffer and twice with kinase buffer (25 mM Tris-Cl [pH 7.4], 20 mM $MgCl_2$, 2 mM $MnCl_2$, 1 mM Na_3VO_4, and 20 μM ATP). ERK2 kinase activity was assayed in 50 μl of kinase buffer containing 10 μCi [γ^{32}P]ATP and 0.2 mg/ml myelin basic protein (MBP). Reaction products were analyzed by SDS-PAGE and quantified with a PhosphorImager.

Acknowledgments

We are grateful to Corie Ralston, Gerry McDermott, and the scientists at beamlines 8.2.1 and 8.2.2, Advanced Light Source (ALS), Berkeley, for assistance with synchrotron data collection. Beamlines 8.2.1 and 8.2.2 at the ALS are supported by the Howard Hughes Medical Institute, and the ALS is supported by the U.S. Department of Energy's Office of Basic Energy Sciences. We are also grateful for support of the beamlines at SSRL (Stanford) and Brookhaven National Laboratories. We thank Tanya Weitze, Greg Bowman, Eric Goedken, Michelle Pirruccello, Michael Hahn, James Keller, and the Bar-Sagi Lab for valuable discussions and assistance. H.S. is supported by the Leukemia & Lymphoma Society. S.M.S. was supported by the Damon Runyon-Walter Winchell Cancer Research Foundation. D.B.-S. is supported by the NIH (grant numbers 5R37 CA55360 and 5P01 CA28146) and J.K. by the NCI (grant number R01 CA096504-02).

Received: May 20, 2004
Revised: August 30, 2004
Accepted: September 2, 2004
Published: October 28, 2004

References

Ahmadian, M.R., Wittinghofer, A., and Herrmann, C. (2002). Fluorescence methods in the study of small GTP-binding proteins. Methods Mol. Biol. *189*, 45–63.

Aronheim, A., Engelberg, D., Li, N., al-Alawi, N., Schlessinger, J., and Karin, M. (1994). Membrane targeting of the nucleotide exchange factor Sos is sufficient for activating the Ras signaling pathway. Cell *78*, 949–961.

Boriack-Sjodin, P.A., Margarit, S.M., Bar-Sagi, D., and Kuriyan, J. (1998). The structural basis of the activation of Ras by Sos. Nature *394*, 337–343.

Brünger, A.T., Adams, P.D., Clore, G.M., DeLano, W.L., Gros, P., Grosse-Kunstleve, R.W., Jiang, J.S., Kuszewski, J., Nilges, M., Pannu, N.S., et al. (1998). Crystallography & NMR system: a new software suite for macromolecular structure determination. Acta Crystallogr. D Biol. Crystallogr. *54*, 905–921.

Buday, L., and Downward, J. (1993). Epidermal growth factor regulates p21ras through the formation of a complex of receptor, Grb2 adapter protein, and Sos nucleotide exchange factor. Cell *73*, 611–620.

Byrne, J.L., Paterson, H.F., and Marshall, C.J. (1996). p21Ras activation by the guanine nucleotide exchange factor Sos, requires the Sos/Grb2 interaction and a second ligand-dependent signal involving the Sos N-terminus. Oncogene *13*, 2055–2065.

Chen, R.H., Corbalan-Garcia, S., and Bar-Sagi, D. (1997). The role of the PH domain in the signal-dependent membrane targeting of Sos. EMBO J. *16*, 1351–1359.

Coleman, M.L., Marshall, C.J., and Olson, M.F. (2004). RAS and RHO GTPases in G1-phase cell-cycle regulation. Nat. Rev. Mol. Cell Biol. *5*, 355–366.

Corbalan-Garcia, S., Margarit, S.M., Galron, D., Yang, S.S., and Bar-Sagi, D. (1998). Regulation of Sos activity by intramolecular interactions. Mol. Cell. Biol. *18*, 880–886.

Das, B., Shu, X., Day, G.J., Han, J., Krishna, U.M., Falck, J.R., and Broek, D. (2000). Control of intramolecular interactions between the pleckstrin homology and Dbl homology domains of Vav and Sos1 regulates Rac binding. J. Biol. Chem. *275*, 15074–15081.

Egan, S.E., Giddings, B.W., Brooks, M.W., Buday, L., Sizeland, A.M., and Weinberg, R.A. (1993). Association of Sos Ras exchange protein with Grb2 is implicated in tyrosine kinase signal transduction and transformation. Nature *363*, 45–51.

Ferguson, K.M., Kavran, J.M., Sankaran, V.G., Fournier, E., Isakoff, S.J., Skolnik, E.Y., and Lemmon, M.A. (2000). Structural basis for discrimination of 3-phosphoinositides by pleckstrin homology domains. Mol. Cell *6*, 373–384.

Gale, N.W., Kaplan, S., Lowenstein, E.J., Schlessinger, J., and Bar-Sagi, D. (1993). Grb2 mediates the EGF-dependent activation of guanine nucleotide exchange on Ras. Nature *363*, 88–92.

Hall, B.E., Yang, S.S., Boriack-Sjodin, P.A., Kuriyan, J., and Bar-Sagi, D. (2001). Structure-based mutagenesis reveals distinct functions for Ras switch 1 and switch 2 in Sos-catalyzed guanine nucleotide exchange. J. Biol. Chem. *276*, 27629–27637.

Hall, B.E., Yang, S.S., and Bar-Sagi, D. (2002). Autoinhibition of Sos by intramolecular interactions. Front. Biosci. *7*, d288–d294.

Hanzal-Bayer, M., Renault, L., Roversi, P., Wittinghofer, A., and Hillig, R.C. (2002). The complex of Arl2-GTP and PDE delta: from structure to function. EMBO J. *21*, 2095–2106.

Kim, J.H., Shirouzu, M., Kataoka, T., Bowtell, D., and Yokoyama, S. (1998). Activation of Ras and its downstream extracellular signal-regulated protein kinases by the CDC25 homology domain of mouse Son-of-sevenless 1 (mSos1). Oncogene *16*, 2597–2607.

Kleywegt, G.J., and Jones, T.A. (1996). Efficient rebuilding of protein structures. Acta Crystallogr. D. Biol. Crystallogr. *52*, 829–832.

Kraemer, A., Brinkmann, T., Plettner, I., Goody, R., and Wittinghofer, A. (2002). Fluorescently labelled guanine nucleotide binding proteins to analyse elementary steps of GAP-catalysed reactions. J. Mol. Biol. *324*, 763–774.

Li, N., Batzer, A., Daly, R., Yajnik, V., Skolnik, E., Chardin, P., Bar-Sagi, D., Margolis, B., and Schlessinger, J. (1993). Guanine-nucleotide-releasing factor hSos1 binds to Grb2 and links receptor tyrosine kinases to Ras signalling. Nature *363*, 85–88.

Margarit, S.M., Sondermann, H., Hall, B.E., Nagar, B., Hoelz, A., Pirruccello, M., Bar-Sagi, D., and Kuriyan, J. (2003). Structural evidence for feedback activation by Ras.GTP of the Ras-specific nucleotide exchange factor SOS. Cell *112*, 685–695.

Milburn, M.V., Tong, L., deVos, A.M., Brünger, A., Yamaizumi, Z., Nishimura, S., and Kim, S.H. (1990). Molecular switch for signal transduction: structural differences between active and inactive forms of protooncogenic ras proteins. Science *247*, 939–945.

Nimnual, A., and Bar-Sagi, D. (2002). The two hats of SOS. Sci STKE 2002, PE36. 10.1126/stke.2002.145.pe36

Nimnual, A.S., Yatsula, B.A., and Bar-Sagi, D. (1998). Coupling of Ras and Rac guanosine triphosphatases through the Ras exchanger Sos. Science *279*, 560–563.

Otwinowski, Z., and Minor, W. (1997). Processing of X-ray diffraction data collected in oscillation mode. Methods Enzymol. *276*, 307–326.

Pai, E.F., Krengel, U., Petsko, G.A., Goody, R.S., Kabsch, W., and Wittinghofer, A. (1990). Refined crystal structure of the triphosphate conformation of H-ras p21 at 1.35 Å resolution: implications for the mechanism of GTP hydrolysis. EMBO J. *9*, 2351–2359.

Qian, X., Vass, W.C., Papageorge, A.G., Anborgh, P.H., and Lowy, D.R. (1998). N terminus of Sos1 Ras exchange factor: critical roles for the Dbl and pleckstrin homology domains. Mol. Cell. Biol. *18*, 771–778.

Silver, S.J., Chen, F., Doyon, L., Zink, A.W., and Rebay, I. (2004). New class of Son-of-sevenless (Sos) alleles highlights the complexities of Sos function. Genesis *39*, 263–272.

Sini, P., Cannas, A., Koleske, A.J., Di Fiore, P.P., and Scita, G. (2004). Abl-dependent tyrosine phosphorylation of Sos-1 mediates growth-factor-induced Rac activation. Nat. Cell Biol. *6*, 268–274.

Soisson, S.M., Nimnual, A.S., Uy, M., Bar-Sagi, D., and Kuriyan, J.

(1998). Crystal structure of the Dbl and pleckstrin homology domains from the human Son of sevenless protein. Cell *95*, 259–268.

Sondermann, H., Soisson, S.M., Bar-Sagi, D., and Kuriyan, J. (2003). Tandem histone folds in the structure of the N-terminal segment of the ras activator Son of Sevenless. Structure *11*, 1583–1593.

Vetter, I.R., and Wittinghofer, A. (2001). The guanine nucleotide-binding switch in three dimensions. Science *294*, 1299–1304.

Worthylake, D.K., Rossman, K.L., and Sondek, J. (2000). Crystal structure of Rac1 in complex with the guanine nucleotide exchange region of Tiam1. Nature *408*, 682–688.

Yarden, Y., and Sliwkowski, M.X. (2001). Untangling the ErbB signalling network. Nat. Rev. Mol. Cell Biol. *2*, 127–137.

Accession Numbers

Crystallographic coordinates and structure factors have been deposited in the Protein Data Bank under accession codes 1XD2, 1XD4, and 1XDV.